



Wide-field-of-view PIV measurements above and below microscale breaking waves

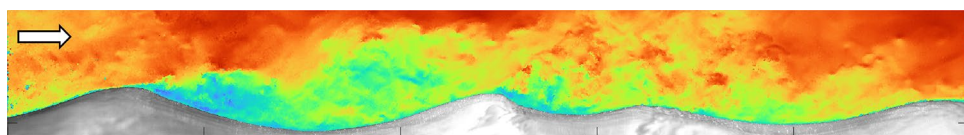
Camille Tondu¹ · Martin Gade² · Julián Morales Meabe² · Marc P. Buckley¹

Received: 8 August 2025 / Revised: 22 September 2025 / Accepted: 6 October 2025
© The Author(s) 2025

Abstract

Small-scale physical processes within the first centimeters above and below ocean surface waves are important for atmosphere-ocean momentum and energy budgets. The complex feedback mechanisms between airflow separation, turbulence under microscale breaking wave crests, and associated parasitic capillary waves remain to be fully understood. A new, 51-cm-wide-field-of-view laser imaging system was developed, which involves high-resolution (one velocity vector every 133 μm) air-water PIV (particle image velocimetry, 33 μm/pixel) and LIF (laser-induced fluorescence, 52 μm/pixel). The system was installed at a fetch of 15.5 m in the 24-m-long, 1-m-wide, 1.5-m-high wind-wave tank of the University of Hamburg (Germany). Wind-generated waves were examined at a reference wind speed of 4.5 m/s. The wide-field-of-view air-side PIV measurements display intense airflow separation events past waves, with sheltering effects that affect several waves downwind. Chronological sequences of air and water-side PIV measurements (11 wide-field-of-view PIV frames per second) allow us to follow the evolution of microscale breaking waves and associated air/water dynamics, and they reveal the intimate coupling between highly intermittent airflow sheltering events, capillary waves, and turbulence below wave crests.

Graphical abstract



1 Introduction

Small-scale dynamics above and below the highly dynamic, wavy surface of the ocean have an important impact on atmosphere-ocean transfer of momentum and scalars

(Wunsch and Ferrari 2004; Sullivan and McWilliams 2010). In particular, airflow separation over steep, microscale breaking waves is believed to strongly influence the air-sea momentum and energy transfers. Microscale breaking waves, arguably ubiquitous over the ocean in the presence of low-to-moderate winds, are short waves with bore-like crests and parasitic capillary waves riding on their forward face (Banner and Phillips 1974; Jessup et al. 1997; Siddiqui et al. 2001). In fact, wave microscale breaking is possibly an important energy dissipation mechanism for the upper ocean, and airflow separation events are believed to significantly modify the air-sea momentum flux, especially in high wind conditions (Melville and Fedorov 2015; Sullivan and McWilliams 2010). Yet the complex coupling mechanisms between highly intermittent airflow separation events and water turbulence within the first millimeters under microscale breaking wave crests remain poorly understood (Sullivan and McWilliams 2010).

✉ Camille Tondu
camille.tondu@hereon.de

Martin Gade
martin.gade@uni-hamburg.de

Julián Morales Meabe
julian.morales.meabe@studium.uni-hamburg.de

Marc P. Buckley
marc.buckley@hereon.de

¹ Institute of Coastal Ocean Dynamics, Helmholtz-Zentrum Hereon, Max-Planck-Straße 1, 21502 Geesthacht, Germany

² Institut für Meereskunde, Universität Hamburg, Bundesstraße 53, 20146 Hamburg, Germany

In recent years, a number of (laboratory) experimental studies have provided important details on the topic. Peirson (1997); Banner and Peirson (1998) pioneered high-resolution particle image velocimetry (PIV) measurements at the air–water interface, as they were able to capture water-side viscous stress under wind waves. Siddiqui et al. (2001, 2004); Siddiqui and Loewen (2007, 2010) were able to quantify turbulence under wind-generated microscale breaking waves and show their important role for energy dissipation. Reul et al. (1999) and later Veron et al. (2007) reported the first PIV measurements of airflow separation over mechanically generated breaking waves and wind waves, respectively. Using coupled PIV and LIF (laser-induced fluorescence) techniques in the airflow over laboratory wind waves, Buckley and Veron (2019) showed that airflow separation can occur past young wind wave crests and contributes to important modulations of surface viscous stress, with a significant drop in stress within the sheltered region (Buckley et al. 2020). This was later confirmed by Tenhaus et al. (2024), who were additionally able to capture along-wave, water-side viscous stress modulations in microscale breaking wave conditions.

Gade et al. (1998) showed that in these conditions, bound (or parasitic) capillary waves (with frequencies ranging from 60 to 100 Hz) are systematically generated past the crest of the steepest, micro-breaking waves (with wavelengths < 30 cm, and frequencies > 2.5 Hz). Theoretical studies have suggested that important nonlinear transfer of energy from the gravity waves to these bound capillaries occurs, and that parasitic capillary waves likely play an important role in wave generation and may delay wave breaking, as they dissipate energy from the dominant waves (Longuet-Higgins 1963; Melville and Fedorov 2015). Numerical studies have also shown that turbulence on both sides of the water interface are significantly modified by capillary wave trains (Deike et al. 2015). However, the very small scale ($O(1$ mm)) at which these phenomena occur renders observational studies difficult. While theories about their

generation (Longuet-Higgins 1992), growth, dissipation (Longuet-Higgins 1963) as well as their possible energy exchanges with the dominant waves (Longuet-Higgins 1963) have been developed, they remain to be verified in controlled laboratory experiments.

Recently, Xu and Perlin (2023) were able to capture bound capillaries and their associated water-side dynamics, albeit for mechanically generated micro-breaking waves, with modified surface tension and without wind forcing. In the presence of wind, however, previous laboratory studies (Banner and Peirson 1998; Reul et al. 2008; Buckley and Veron 2017; Tenhaus et al. 2024) were unable to fully resolve the evolution of bound capillary waves at the crests of wind waves, and related coupled air–water flow kinematics.

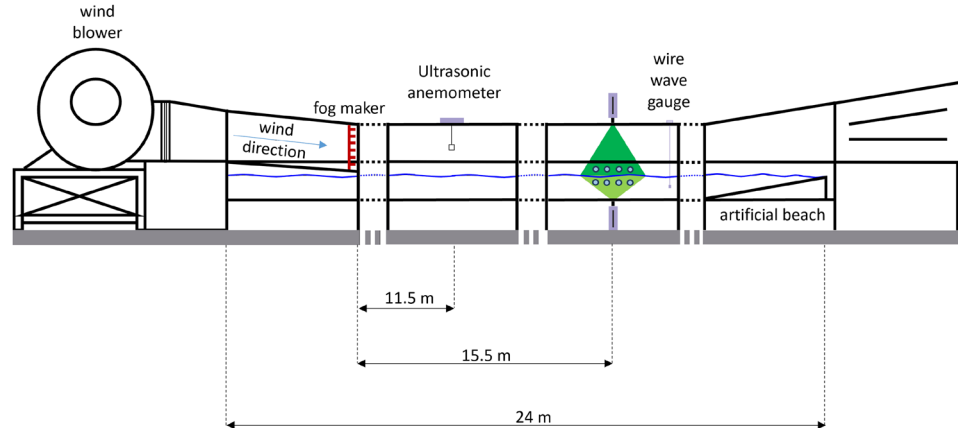
In this work, a new laser imaging system is presented, which involves air- and water-side PIV and LIF measurements with unprecedented resolution and width of field of view. Then, results from laboratory experiments on wind-generated waves conducted at a reference wind speed of 4.5 m/s (measured at a height of 64 cm above the mean water level) are presented and discussed, thereby demonstrating the unique capability of the system to capture the detailed evolution in time and space of airflow separation events, microscale wave breaking, and parasitic capillary waves.

2 Methods

2.1 Experimental setup

The experiments were carried out at the wind-wave tank of the University of Hamburg, Germany (Fig. 1), located at the Federal Waterways Engineering and Research Institute (Bundesanstalt für Wasserbau), Germany. The water-filled section is 24 m long, 1 m wide, 51 cm deep, and the air space is 1 m high. The tank was filled with freshwater. A radial blower generates reference wind speeds up to approximately

Fig. 1 Schematic of the large wind-wave facility of the University of Hamburg (Germany)



10 m/s, measured by an ultrasonic anemometer (Trisonica Mini Wind Weather Sensor, Anemoment) at a height of 64 cm above the mean water surface. A beach with a 1:7.2 slope prevents the reflection of waves back into the study section.

A single-point sensor provides characteristics of the wave field: A time series of the elevation of the water surface is measured using a resistance-type wire wave gauge with a spectral resolution of about 30 Hz (Lobemeier 1981) located at a fetch of 16 m.

A wide-field-of-view laser imaging system, combining PIV and laser-induced fluorescence (LIF) techniques, was installed approximately 1 m before the beginning of the beach, at a fetch of 15.5 m, where the wind waves are sufficiently developed and display realistic groupiness. Details are provided in the following subsection.

2.2 Wide-field-of-view PIV and LIF system

A multi-camera, multi-laser, wide-field-of-view laser imaging system was developed for this study, capable of performing high-resolution velocity measurements above and below a train of several short wind waves. The setup combines the use of PIV, to capture the motions in the air and in the water flow, with LIF, to accurately detect the water surface.

A schematic of the system is provided in Fig. 2. Two Nd:YAG PIV lasers (Quantel Evergreen, 200 mJ per pulse, 532 nm, <10 ns pulse duration) were positioned vertically above and below the tank, respectively (Fig. 2a). The top, downward flashing (resp. bottom, upward flashing) laser was used for air-side (resp. water-side) PIV (and simultaneous LIF water surface elevation measurements). Each laser head was fitted with light sheet optics (Dantec Dynamics), which were set to produce a light sheet with a thickness of 2 mm.

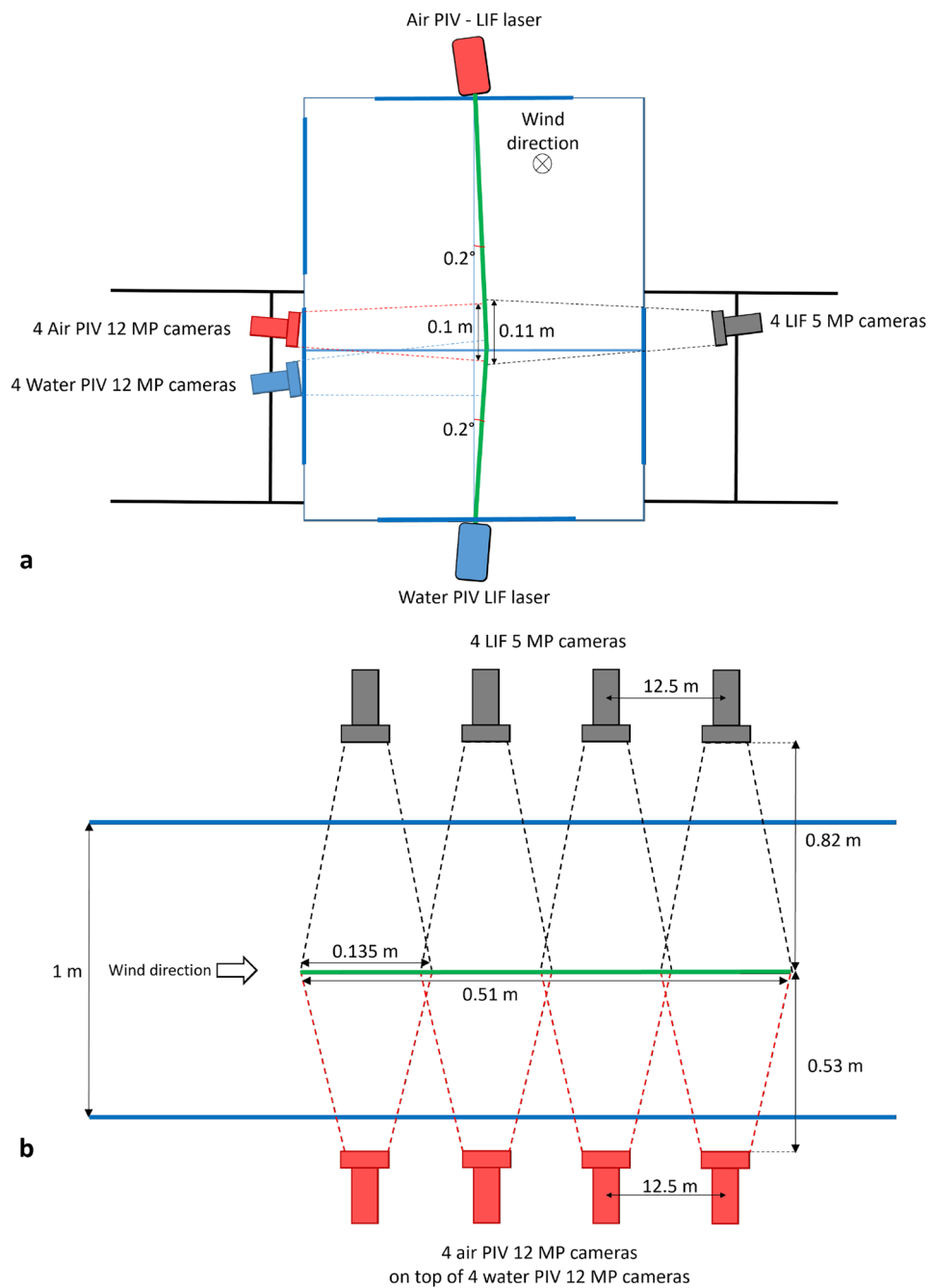
A total of 12 industrial CMOS cameras were utilized to capture velocities in the air and in the water (PIV), as well as spatial snapshots of the water surface (LIF). For the air-side (resp. water-side) PIV, four 12 MP cameras (Flare CXP 12M180, resp. Victorem CXP 120B68, IO Industries) fitted with 85 mm (resp. 50 mm) Canon EF lenses were mounted side by side, forming a horizontal array (Fig. 2b). Each PIV camera had a 13.5-cm-wide, 10-cm-high field of view, with a 1-cm overlap with its neighboring camera. After image correction and stitching of the images (see below), this resulted in a 51-cm-wide field of view. With a raw PIV image resolution of 33 $\mu\text{m}/\text{pixel}$, the final velocity resolution was one velocity vector every 133 μm^2 . The PIV cameras acquired images at a rate of 22 frames per second (fps), yielding 11 wide-field-of-view 2D PIV velocity fields per second. Each PIV camera lens was fitted with a green acrylic bandpass optical filter (Laservision P1H09, with an optical density (OD) larger than 1 at 532 nm), to reduce optical noise. Both sides of the water interface were seeded with passive tracer

particles. In the air, particles with a diameter of 8 to 12 μm were generated by an industrial fog generator (Aft GmbH) equipped with 45 misting nozzles, installed at 0-m fetch. For the water-side PIV, hollow glass particles with a diameter of 8 to 13 μm were mixed into the water. For the conditions shown in this paper ($U_{64\text{cm}} = 4.5 \text{ m/s}$), the time interval between two images of one PIV pair (PIV Δt) was set to $\Delta t = 200 \mu\text{s}$ for air-side PIV, and $\Delta t = 2 \text{ ms}$ for water PIV. One LIF frame was recorded per PIV frame. It was ensured that the Stokes number τ_p/τ_η was small enough ($S_t \ll 1$) in both fluids so that the particles accurately followed the fluid streamlines. On the air side (resp. the water side), the particle relaxation time $\tau_{p,a} = \sim 0.44 \text{ ms}$ (resp. $\tau_{p,w} = \sim 10.3 \mu\text{s}$) was ~ 36 times (resp. ~ 59242 times) smaller than the estimated Kolmogorov time scale $\tau_{\eta,a} = \sim 16 \text{ ms}$ (resp. $\tau_{\eta,w} = \sim 782 \text{ ms}$).

On the raw, water-side PIV images, direct detection of the surface was difficult. Therefore, four 5 MP cameras (Victorem CXP 51B163, IO Industries), fitted with 50 mm lenses, were mounted on the other side of the tank, to produce sharp images of the wavy interface through LIF. Each LIF camera had a 13.5-cm-wide, 11-cm-high field of view. With a 1-cm overlap between adjacent frames, this resulted in a 51-cm-wide field of view. The LIF spatial resolution was 55 $\mu\text{m}/\text{pixel}$. These cameras were operated at the same frame rate as the PIV cameras were (22 fps) and used, as a light source, the same laser sheet as the PIV cameras did. Rhodamine 6G dye was mixed into the water at a concentration of approximately 10 $\mu\text{g/L}$. When excited by the green laser light ($\lambda = 532 \text{ nm}$), the Rhodamine emits fluorescent light at a wavelength of $\lambda = 564 \text{ nm}$. The LIF cameras were fitted with amber acrylic high-pass optical filters (Laservision P1N01, with OD ≥ 5 for wavelengths below 535 nm), thereby filtering out the green light scattered by the PIV tracer particles, but not the fluorescence (e.g., Buckley and Veron 2017; Tenhaus et al. 2024), as shown in Fig. 3a. Accurate surface detection was straightforward on those images (as shown in Panel a), and these were matched on the raw water PIV data to create the masks necessary for the data processing. The surfaces were directly detected on the Air PIV raw data (Panel c). Panels d and e show an enlarged version of the region near the crest of the wind wave, where parasitic capillary waves are well resolved by the LIF and air PIV surface detection technique.

The lasers were tilted 0.2° from the vertical, away from the PIV cameras to reduce the probability of direct reflections from the surface. The cameras were also tilted, 7.7° downward for the air PIV and LIF cameras, and 8.3° upward for the water PIV cameras, to avoid shadowing effects by waves between the field of view and the tank window (Buckley and Veron 2017; Tenhaus et al. 2024).

Fig. 2 PIV-LIF setup, crosswind view (**a**) and top view (**b**)



All 12 PIV cameras and 2 PIV lasers were controlled and triggered using National Instruments Software (LabVIEW) and hardware (PCIe-6612 counter/time modules). Window wipers, installed on the windows of the tank, were operated between acquisition runs to clean any accumulated fog, and clear the optical paths of the LIF and air-side PIV cameras, and of the top laser. Raw PIV and LIF images were recorded using 4 digital video recorders (Express Core 2 Max, IO Industries), together with video recording software (Streams 7, IO Industries). The

images were subsequently transferred to hard disk drives for processing.

2.3 Image processing

Prior to computing velocity vectors in both the air and water phases, a series of image processing steps were performed using MATLAB (MathWorks). First, images from all 12 cameras were dewarped to correct for their angle of tilt, and projected into Cartesian coordinates. The images were then stitched together along their adjacent, overlapping edges,

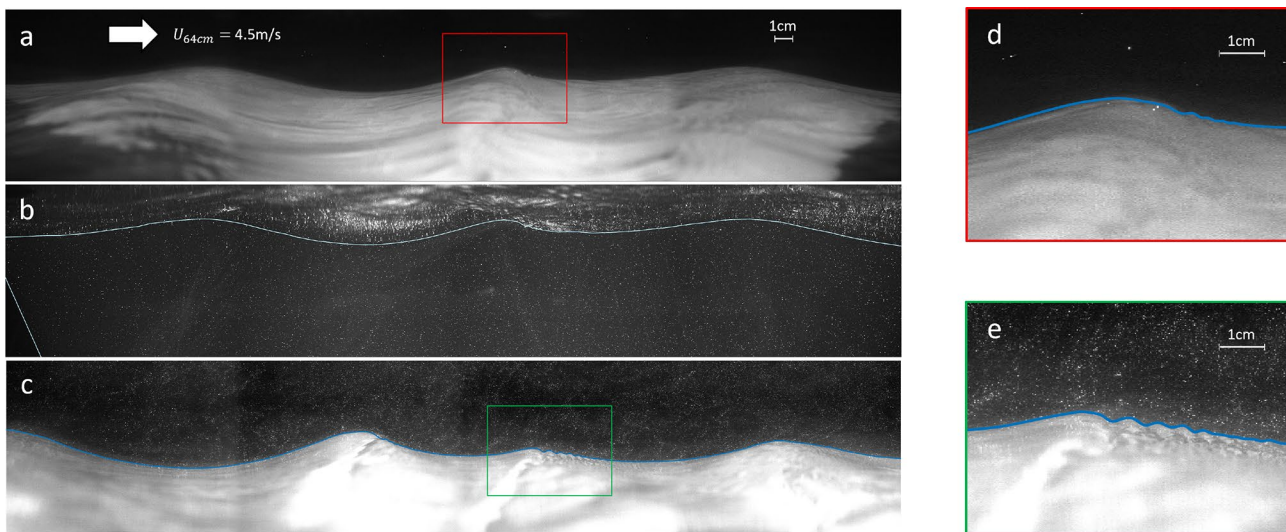


Fig. 3 **a** Raw LIF image, **b** Raw water-side PIV image, with the detected surface from the corresponding LIF image, **c** Example of raw air PIV image, with the detected surface, **d** Enlarged portion of

the LIF image (**a**), with visible parasitic capillaries, **e** Enlarged portion of the air PIV image (**c**), with visible parasitic capillaries

to form wide-field-of-view images. The air–water interface was automatically detected on the raw LIF images, using image segmentation software developed by Kirillov et al. (2023). The LIF surfaces were then transferred to the raw water PIV images and used to mask out areas that are above the surface (Fig. 3c). For the masking of the air PIV images, the air–water interface was directly detected on the raw PIV images, without using the LIF data, as the segmentation algorithm showed good results in accurately locating the surface despite the presence of tracer particles.

The dewarped, stitched, and masked wide-field-of-view air and water PIV images were then processed for the calculation of velocity vectors, using DynamicStudio software (Dantec Dynamics). The PIV algorithm, which relies on a pyramid cascade principle (Thomas et al. 2005), was used with a final interrogation window of 8x8 pixels, with a 50% overlap.

3 Results and discussion

In this section, we show examples of results obtained in moderate wind conditions ($u_{ref} = 4.5$ m/s) that illustrate the unique ability of the measurement system to capture the details and evolution in time of air, water, and water surface dynamics. The wind waves studied are steep and young, with an apparent peak wave steepness $\gamma_p = 0.31$, an apparent peak frequency $f_p = 2.85$ Hz, and a wave age $c_p/u_{*a} = 2.27$, where c_p is the apparent peak wave speed derived from the wire wave gauge time series. u_{*a} , the friction velocity in the air,

was obtained by extrapolating a linear fit of the mean turbulent stress profile down to the surface, $u_{*a} = 0.242$ m/s (see, for example, (Cheung and Street 1988), who used a similar methodology). Details on the estimation of the turbulent stress are provided in the following section.

3.1 Time evolution of air and water-side kinematics throughout wave steepening and flattening events

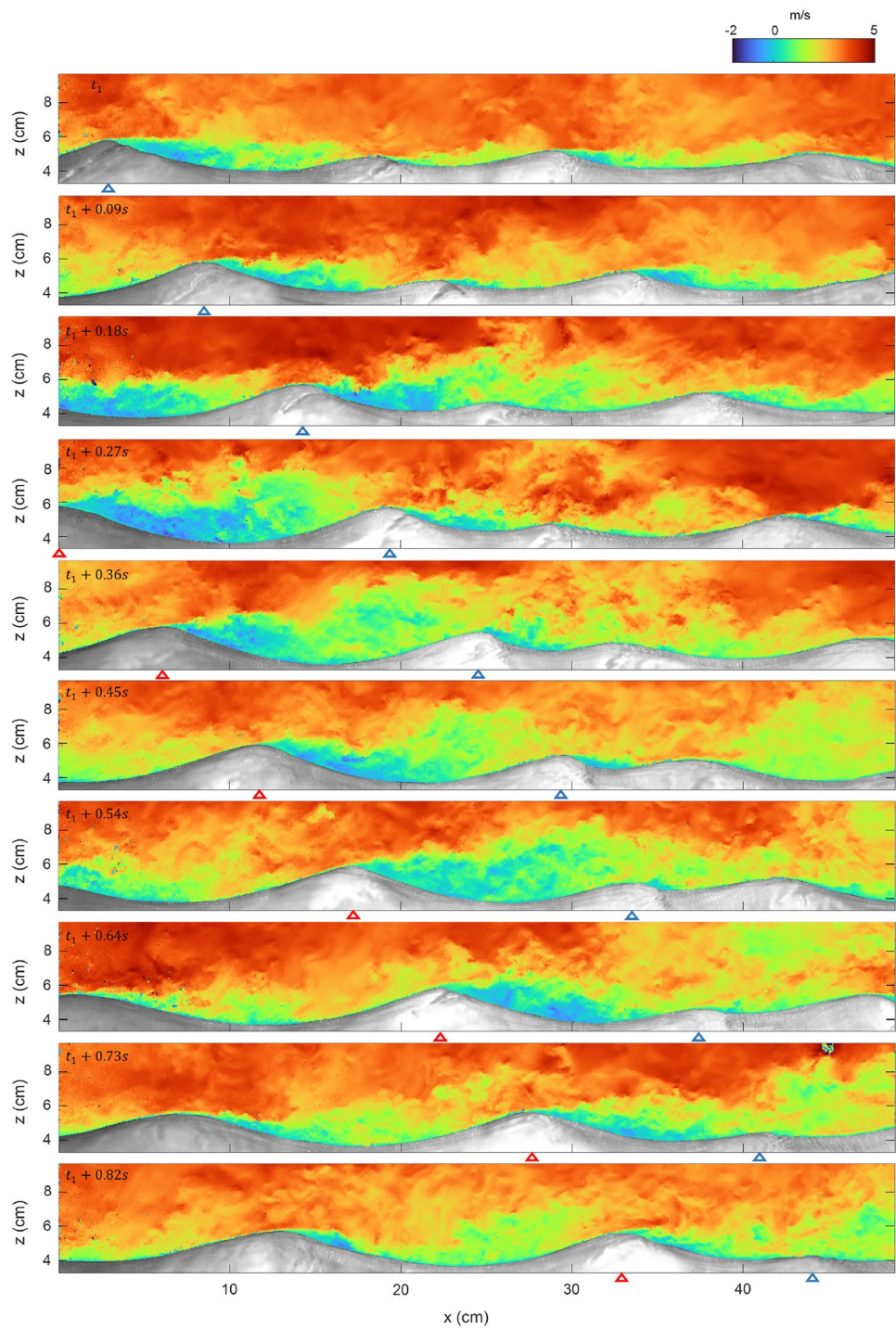
3.1.1 Air side

Since the wide PIV field of view is able to capture multiple waves at a time, we can follow the evolution and propagation of individual waves, and their associated airflow and water dynamics. In Fig. 4, we show a chronological sequence of air-side PIV fields (only the horizontal velocity component is shown) over a period of 0.82 s.

For clarity, we have marked one of the waves with a blue triangle during the entire time interval, and the following wave with a red triangle (starting at time $t_1 + 0.27$ s).

The sequence of velocity fields shows that the waves significantly modulate the airflow. In fact, at time t_1 , for example, the streamwise velocity is high above the crest of the blue-marked wave, and drops significantly past the crest, where it even becomes negative. The young, slow, strongly wind-forced wave is acting as an obstacle (such as a hill) and shelters the region past its crest. This phenomenon is known as a separated sheltering event, or airflow separation Jeffreys (1925); Belcher and Hunt (1998). In fact, we observe sheltering events (separated and non-separated) past

Fig. 4 Chronological sequence of wide field-of-view air-side PIV fields, instantaneous horizontal velocity component u



the crests of nearly all the waves shown in this figure. In the cases where separation takes place, the airflow boundary layer detaches from the surface just past the crest of a wave and generally reattaches on the windward side of the next wave (see, for example, the blue-marked wave at times t_1 and $t_1+0.09$ s). This observation is consistent with previous laboratory and field studies (e.g., Buckley and Veron 2016; Buckley et al. 2020; Buckley 2015). Here, however, thanks

to the unprecedented width and resolution of the field of view, we are able to directly observe, instances where the sheltered region extends beyond the crest of the next wave, only to reach the windward face of the following one. This is apparent at $t_1+0.18$ s, where the blue-marked wave causes the airflow to “skip” the small wave just downwind of it. This is, to the best of our knowledge, the first direct observation of such an event.

This phenomenon is evidently highly intermittent; since an instant later ($t_1 + 0.27$ s), the size of the sheltered region decreases significantly. At the same time, the red-marked wave, located upwind of the blue-marked wave, creates a large sheltered event, causing a large region of reduced velocities and increased variability. At $t_1 + 0.36$ s, this sheltered region appears to merge with the sheltered regions above the two next waves, producing a large sheltering event that extends nearly up to the right edge of the field of view. This effect is short-lived, as it subsides 0.09 s later, at $t_1 + 0.45$ s.

Then, from $t_1 + 0.54$ s to $t_1 + 0.82$ s, the blue-marked wave appears to be intermittently within the sheltered region caused by the red-marked wave. It should be mentioned that since we can follow individual waves over multiple images, the speed of an individual wave can be readily obtained from the provided sequence. Here, the blue-marked wave travels at a speed above 0.6 m/s at t_1 and decelerates rapidly to reach approximately 0.3 m/s 0.82 s later. In fact, the height of the blue wave also decreases until the wave almost disappears at $t_1 + 0.82$ s, yet capillary waves remain clearly visible near its crest. Therefore, the system offers the ability to not only examine the effects of air- and water-side dynamics on the development and breaking of gravity-capillary waves, but also the influence of wave groups and associated modulations of individual waves as they travel through individual wave packets.

3.1.2 Evolution of individual wave crest geometry

In order to evaluate the complex coupling mechanisms between wind stress, water-side turbulence, and microscale breaking events, it is important to resolve microscale roughness elements at the water surface. This is especially critical in the near crest region, where parasitic capillary waves are believed to interact with the air and water turbulence. In an effort to connect the observed airflow kinematics over individual waves (shown in Fig. 4) with their microscale surface geometry features, we now examine the ability of the

imaging system to resolve surface slope and capillary waves along the dominant waves.

As shown in Fig. 3 (Panels d,e), the raw LIF and PIV images resolve well the geometry of the water surface, including capillary waves near the crests of the dominant waves. In Fig. 5, we show an example LIF surface $\eta(x)$ (panel a), and its associated slope $\partial\eta/\partial x$ (panel b). Important slope variations are clearly visible near the crests of the dominant waves, where capillary waves are present. However, the slope signal is a function of both dominant and capillary wave geometry, rendering a systematic identification of capillary waves difficult. In order to systematically identify the presence, or absence, of parasitic (bound) capillary waves in the vicinity of the wave crests above (resp. below) which we measure air-side (resp. water-side) kinematics, an empirical mode decomposition (EMD) of the LIF surfaces is performed, following the methodology used by Xu and Perlin (2023). Thanks to a sifting process, the EMD can decompose the instantaneous surface $\eta(x)$ into a sum of oscillatory components called intrinsic mode (IMF) functions (noted here $\eta_n(x)$), and a monotonic function (residue) $r(x)$ (Zeiler et al. 2010):

$$\eta(x) = \sum_n \eta_n(x) + r(x) \quad (1)$$

First, the envelopes of the primary signal $\eta(x)$ are computed. Then, their means are subtracted from the original surface. To be validated as an IMF, the number of local minima and maxima of the resulting signal has to differ at most by one and its mean has to be zero. If these two conditions are not fulfilled, the sifting process continues with the previous signal as input signal. Otherwise, the IMF mode is stored. Finally, if the function resulting from the subtraction of the IMF mode from the input signal is monotonic, it is identified as the residue ($r(x)$) in Eq. 1 and the algorithm stops. Otherwise, the procedure restarts with this function as the input signal (Zeiler et al. 2010). Using this method, we are able to subtract the capillaries (highest frequency signal which corresponds to the first mode of the EMD, see Fig. 5c), from the

Fig. 5 Empirical mode decomposition (EMD) of the surface. **a** Instantaneous surface. **b** Horizontal surface gradient. **c** First intrinsic function mode (IMF) of the EMD. **d** Sum of the other IMFs (from 2nd to 5th)

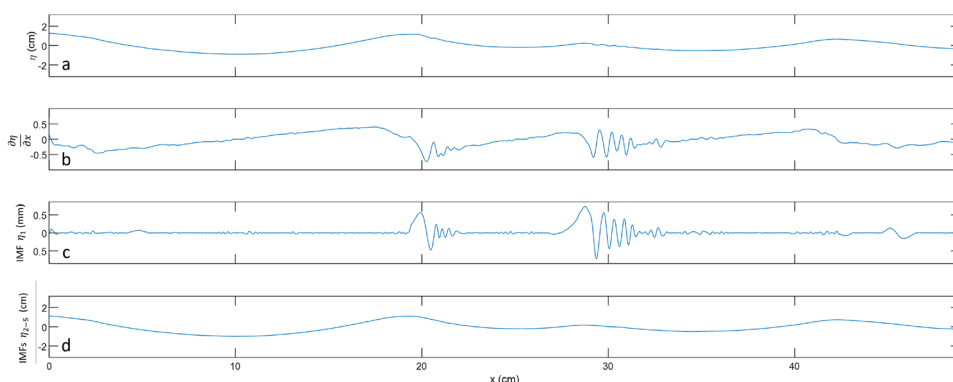
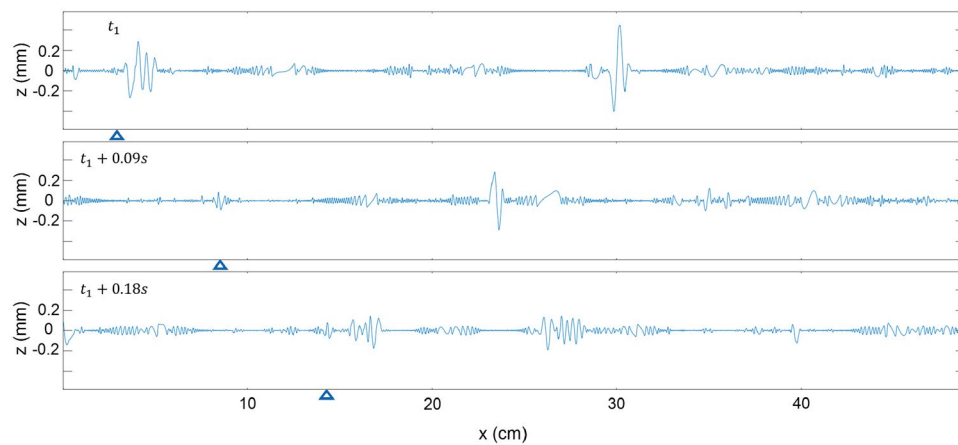


Fig. 6 First intrinsic mode function (IMF) of the surface EMD, corresponding to the 3 first PIV snapshots of Fig. 4



primary waves (contained in the remaining lower frequency modes, shown in panel d).

In Fig. 6, we show the first IMF corresponding to the surface of the first three air PIV snapshots from Fig. 4. At t_1 , the first and third waves seem to be steep enough to generate a capillary wave train past their crests. These are represented by the high-amplitude oscillations in the first mode of the EMD. The small amplitude variability is assumed to be noise.

At $t_1 + 0.09$ s, airflow separation still occurs past the crest of the first wave (Fig. 4) but no capillaries are detected past the crest (Fig. 6). This is also the case past the last dominant wave at $t_1 + 0.09$ s. This observation points to the complexity of airflow separation dynamics over wind waves. While past studies have suggested that airflow separation can only take place over breaking waves (Banner and Melville 1976; Gent and Taylor 1976), more recent measurements have shown airflow separation events over microscale breaking waves, (Buckley and Veron 2017; Buckley et al. 2020).

3.1.3 Water side

As described in the Methods section above, water-side PIV measurements were achieved in the same conditions as the air-side PIV. In Fig. 7, we show a sequence of wide-field-of-view water-side PIV snapshots (horizontal velocity component), taken within a time interval of 0.73 s. We observe that the orbital velocities of the dominant waves dominate the velocity field, with positive horizontal velocities measured below crests, and negative velocities below troughs. Here, we follow the evolution of the highest, steepest wave (labeled by a blue triangular marker). This wave, traveling on average at 0.55 m/s, displays high velocity values (~ 0.5 m/s) just below its crest. From t_2 to $t_2 + 0.36$ s, the wave grows and the horizontal velocity below its crest gradually increases.

At $t_2 + 0.45$ s, the wave is skewed to the right and there is a bulge, prior to the formation of the capillaries. This instant is further investigated in Section 3.2.2.

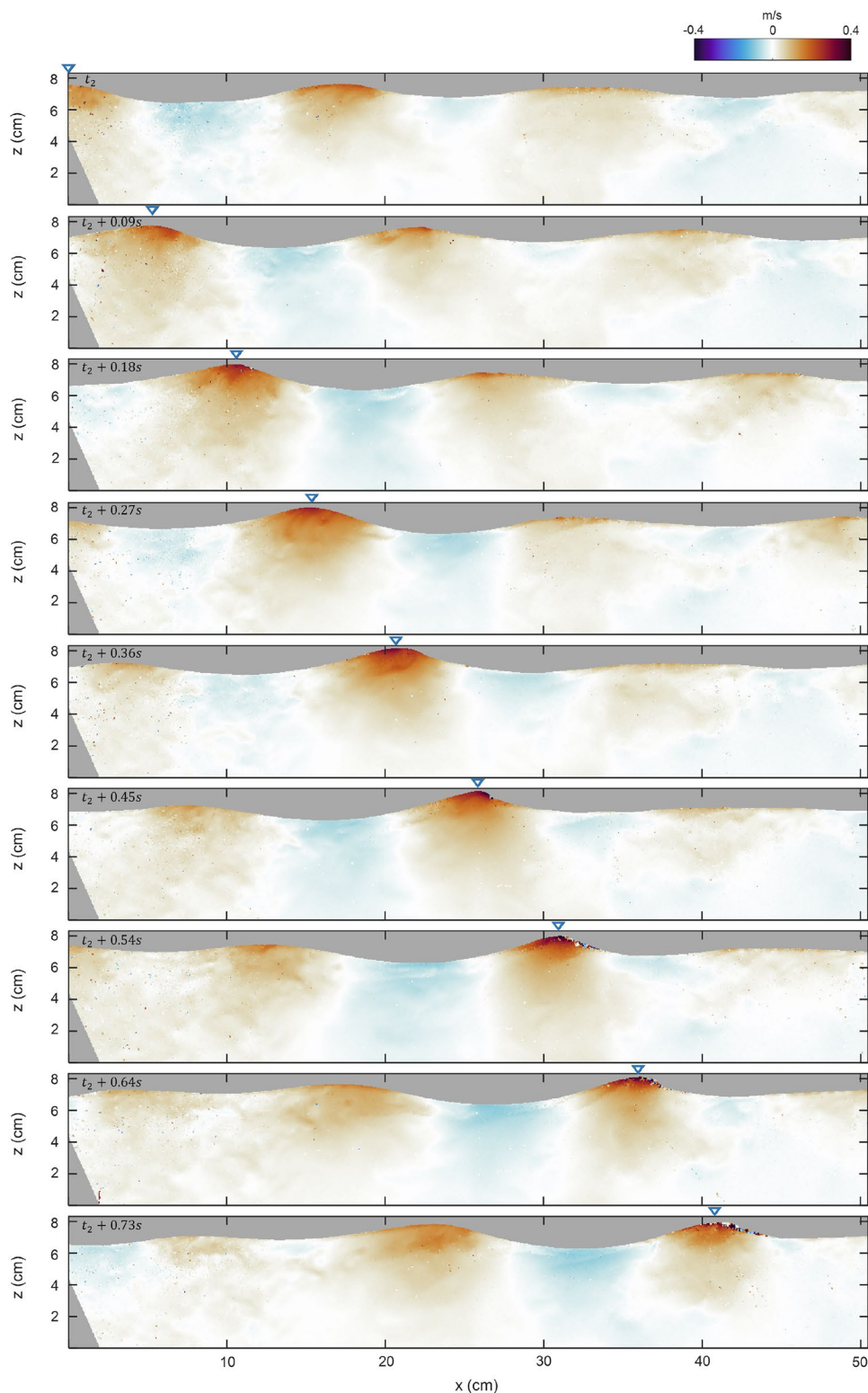
From $t_1 + 0.54$ s to $t_1 + 0.73$ s, as the wave evolves to the end of the field of view, parasitic capillary waves are generated. Strong positive and negative horizontal velocity patches are visible under the capillaries, an indicator of a strong mixing in this particular region. This observation is in general agreement with past numerical, observational and theoretical studies of steep, microscale breaking waves (Deike et al. 2015; Ebuchi et al. 1987; Longuet-Higgins 1992). We note here that the wave upwind of the blue-marked wave gradually steepens with time, while the wave downwind becomes flatter. This is likely due to the modulation of these deep water wind waves by the wave group, whereby individual waves steepen, (microscale) break, and flatten as they travel through a group. However, as shown above, these changes in wave geometry are usually coupled with rapidly varying, turbulent sheltering events, which may in turn control how momentum is partitioned between turbulent, wave-induced, and viscous contributions, to be ultimately transferred to the waves and surface currents (Buckley et al. 2020).

3.2 Viscous, turbulent, and wave-induced dynamics above and below the water surface

3.2.1 Air-side PIV measurements

In Fig. 8, we focus on the instantaneous airflow velocity field, acquired above a train of 3 wind waves. As in the sequence of velocity fields from Fig. 4, the horizontal velocity field shown here (Panel a) displays clear signs of sheltering past the crests of all three waves. In fact, the vertical velocities (Panel b) are largely consistent with sheltering dynamics. Over the first, steeper wave, the airflow broadly moves upward upwind of the crest, and downward downwind, but with increased variability near the surface

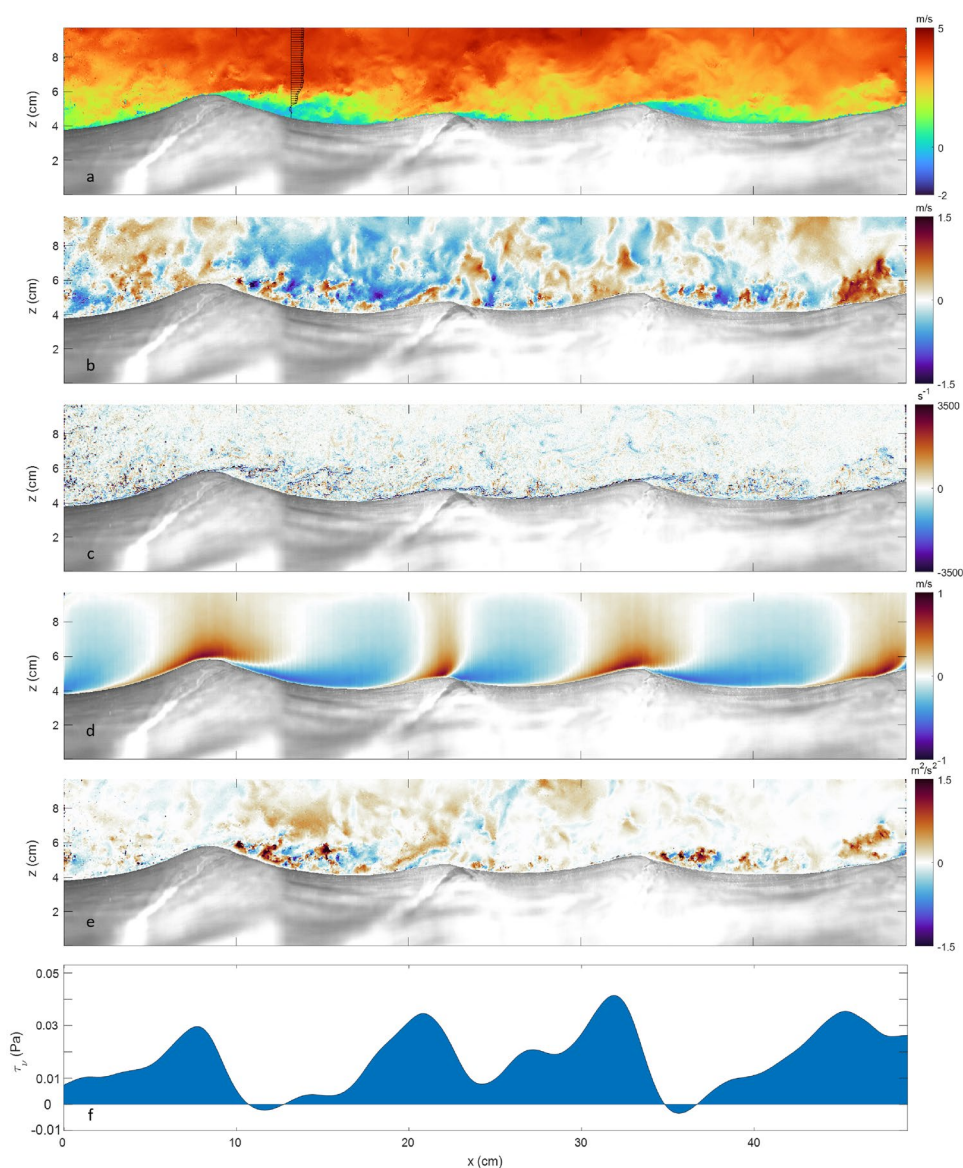
Fig. 7 Chronological sequence of water-side PIV velocity fields, instantaneous horizontal velocity component u



on the leeward side, i.e., within the sheltered region. Past the second wave and up to the right-hand edge of the snapshot, the vertical velocities show important variability, possibly caused by the pronounced airflow separation event over the first wave. Nonetheless, the following waves also

modulate the airflow, as upward motion can be observed just before the crest very near the surface, as well as alternating upward–downward motions within the sheltered regions of the second and third waves.

Fig. 8 Airflow dynamics above a train of 3 wind waves, **a** instantaneous horizontal velocity component u (m/s), **b** instantaneous vertical velocity component w (m/s), **c** spanwise vorticity ω (s^{-1}), with negative vorticity in the clockwise direction, **d** wave-induced horizontal velocity \tilde{u} (m/s), **e** turbulent stress $-u'w'$ (m^2/s^2), **f** surface viscous stress τ_v (Pa)



The observation of airflow separation over the first, steep wave is in general agreement with past measurements with narrower fields of view (Buckley and Veron 2017). Here, however, thanks to the wide field of view, we can demonstrate that the high variability observed within the right-hand (downwind) portion of the field is influenced by the airflow separation event taking place above waves farther upwind. This suggests that the position of a wind wave within the group likely has an impact on the wind-induced momentum and energy fluxes into that wave. The instantaneous spanwise vorticity (Panel c), a Galilean invariant, unequivocally confirms that all three waves observed here are causing airflow separation: a high (negative) vorticity layer is present on the windward side of the waves, which is characteristic of an attached boundary layer. Past the crest of the waves, this high vorticity layer detaches from the surface, then

disintegrates, and is finally regenerated on the windward face of the next wave. After the separation point, close to the surface, the vorticity is either considerably reduced or is even slightly positive in the region over which airflow reversal happens. The detached, free high-vorticity layers disintegrate into high-magnitude negative and positive vortices, which are shed away from the top of the wave crests.

Reul (1998) suggested that the vortices caused by airflow separation events can be advected several wavelengths downwind of mechanically generated (spilling) breaking waves that they studied. Here, our wide field of view allows us to directly observe that vorticity structures caused by airflow separation over wind waves can also extend farther downwind than 1 wavelength, and that the created wakes can even overcome the following waves, directly influencing the airflow structure above them. This is particularly visible if

one follows the negative vorticity layers ejected away from the surface, past the crest of the first wave.

In order to compute turbulent and wave-coherent velocities, a triple decomposition of instantaneous velocities was performed. The instantaneous horizontal velocity component can be written as $u = \langle u \rangle + u' = \bar{u} + \tilde{u} + u'$, where $\langle u \rangle$ is the phase averaged velocity field, \bar{u} the mean velocity profile, \tilde{u} the wave-induced component and u' the turbulent velocity. Phase averages are produced the same way as described by Buckley and Veron (2016) and Tenhaus et al. (2024): First, a Hilbert transform of the surface data, $\mathcal{H}\{\eta(x)\}$, is computed for each wide-field-of-view frame, with

$$\mathcal{H}\{\eta(x)\} = \frac{1}{\pi} P.V. \int_{-\infty}^{\infty} \frac{\eta(x')}{x - x'} dx' \quad (2)$$

where P.V is the Cauchy principal value of the integral. This is done using MATLAB's *hilbert* function, which makes use of the fact that the Fourier transform of the Hilbert transform of a signal is equal to two times its Fourier transform (e.g., Melville 1983, their equations 2.1–2.8). The phase domain (from 0 to 2π) is divided into 72 bins. Data corresponding to a specific phase are then averaged together (conditional averaging). The algorithm is run for both surface elevation data and velocities. For this study, averages were performed over 660 2D PIV velocity fields for both air and water cases. Each 2D velocity field consists of over 2.7 million vectors.

The resulting wave-induced velocities (horizontal component, Fig. 8d) reflect the wave-induced modulations of the airflow, with alternating positive and negative patterns. Close to the surface, the velocity contours are tilted downwind and are positive above the windward side of crests and negative above the leeward side. Away from the surface, regions of positive (resp. negative) \tilde{u} are found above crests (resp. troughs). This pattern is in good agreement with past laboratory measurements (Buckley and Veron 2016, 2019) and numerical simulations (Sullivan et al. 2000).

The instantaneous turbulent flux field $-u'w'$ (Fig. 8e) carries the signature of the airflow separation taking place past the crests of the three waves. The positive and negative velocity perturbations within the sheltered region are significant in that they exceed the mean, wave-induced velocity reduction that takes place on average downwind of crests.

Intense negative and positive turbulent stresses (Fig. 8e) are visible above the leeward side of the waves: The airflow separation enhances the production of turbulent shear. This result is in general agreement with past observations of airflow kinematics over single wave crests (Tenhaus et al. 2024; Buckley and Veron 2016, 2017). Here, with a spatial snapshot of turbulence over 3 consecutive waves, we can directly observe the substantial spatial variability of the turbulence, from one wave to another. We observe intense turbulence above the lee of the first, steepest wave, followed

directly by reduced turbulence over the small, second wave, and again an important increase on the lee of the third wave. These phase-locked features point toward the likely important role of turbulent (sheltering) events for energy transfer between wind and waves (Belcher and Hunt 1998; Buckley et al. 2025).

The surface viscous stress (or viscous momentum flux, Fig. 8f) is given by

$$\tau_v = \mu \left(\frac{\partial u_t}{\partial \zeta} + \frac{\partial w_n}{\partial \xi} \right) \quad (3)$$

where μ is the air or water dynamic viscosity, and u_t and w_n are the velocity components projected in the ζ and ξ directions, which are, respectively, tangential and normal to the instantaneous surface $\eta(x)$ (Buckley and Veron 2016). Here, only the first measured velocity vectors within the viscous boundary layer were used, and the results were smoothed via a cubic spline method.

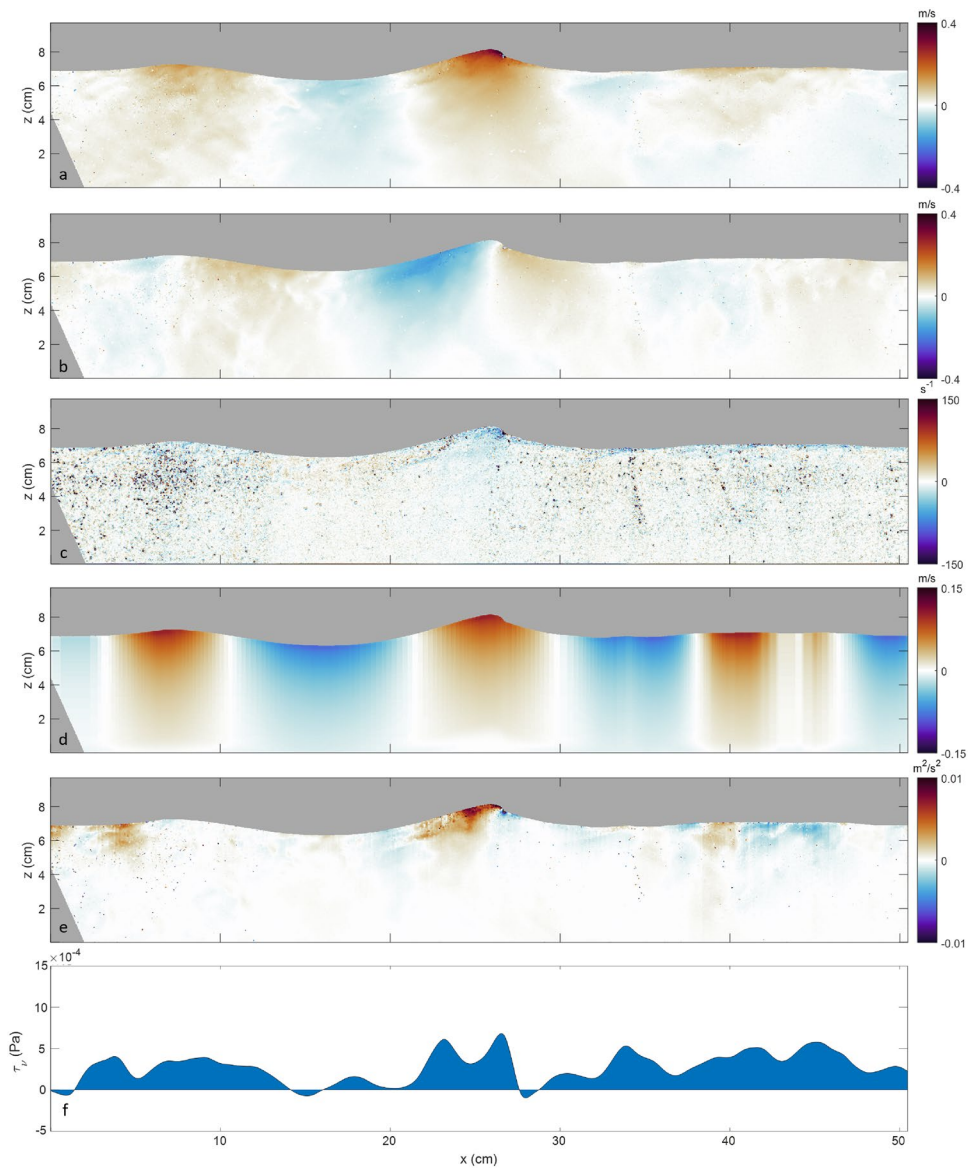
We observe important along-wave modulations of the viscous stress. It reaches a maximum slightly upwind of the wave crests and a minimum downwind of the crest. The viscous stress even reaches negative values downwind of the first and third waves, where air flow reversal was observed (Panel a). This means that at those locations of the surface, momentum is transferred from the water to the air. While the observed pattern agrees well, once again, with previous measurements (Tenhaus et al. 2024; Buckley et al. 2020), the wide field of view allows us to begin looking at the influence of neighboring wind-wave kinematics on individual waves. Here, we note that the second (smaller) wave experiences intense viscous stress just windward of its crest, in spite of being less steep and less high than its upwind neighbor, for example. A possible explanation is the intense downward sweep of high velocity airflow just downwind of the airflow separation event past the first wave's crest (Panel a).

3.2.2 Water-side PIV measurements

In Fig. 9, we examine in detail the water-side dynamics observed at $t_2 + 0.45$ s (from Fig. 7). The instantaneous horizontal (Panel a) and vertical components (Panel b) of the velocity are broadly consistent with orbital motions of linear waves (e.g., Kundu and Cohen 2004). Both plots show that the magnitude of these motions is high near the surface but rapidly decreases with increasing depth. The wave-coherent velocity contours (Fig. 9d) further support this agreement, with positive \tilde{u} below crests, and negative values below troughs.

The relatively steep wave in the middle of the field of view has similar geometrical characteristics as the airflow separating waves observed above. Therefore, we assume that

Fig. 9 Water dynamics below a train of 3 waves, **a** instantaneous horizontal velocity component u (m/s), **b** instantaneous vertical velocity component w (m/s), **c** vorticity ω (s^{-1}), **d** wave-induced horizontal velocity \tilde{u} (m/s), **e** turbulent stress $-u'w'$ (m^2/s^2), **f** surface viscous stress τ_v (Pa)



this wave is also causing airflow separation. In fact, the wave exhibits a bulge at its crest and is skewed to the right.

This bulge (or toe) is likely a source of instabilities according to the theoretical work of Longuet-Higgins (1992) and precedes the generation of parasitic capillaries (see also again Fig. 7, at time $t_2 + 0.54$ s, i.e., 0.09 s later, where capillaries are indeed observed). Underneath the crest, the horizontal velocity magnitude is particularly strong.

The vorticity map (Fig. 9c) is somewhat noisy, especially on the left side of the field of view. On the right side of the image, 2 lines of positive and negative vorticity tilted to the right are assumed to be due to artifacts produced by laser light reflections.

The crest of the steep, middle wave is dominated by negative vorticity, except below the forward face of the toe, where a small region of high positive vorticity is

detected. Directly behind this area, strong negative vorticity is being produced and seem to diffuse along the crest to the windward side of the wave. Xu and Perlin (2023), in their study of small, mechanically generated waves, also observed vorticity below capillaries, in particular strong negative vorticity below troughs, and weak positive and negative vorticity below the crest of the parent wave. Here, the observed positive vorticity is comparatively somewhat shifted downstream and much more intense. Negative vorticity is prevalent below the leeward side of the wind wave shown here, even though capillaries have not yet formed. While the vorticity below the capillaries of mechanically generated waves of Xu and Perlin (2023) was advected downstream, here, the vorticity seems to propagate upwind, suggesting that additional effects due to the wind drift layer are probably modifying the underwater

dynamics. In addition, thanks to our ability to track vorticity structures over the width of our field of view, we can directly observe that vorticity produced under a wave crest does not extend beyond one dominant wavelength, as was hypothesized by Siddiqui and Loewen (2010). This is in contrast with the air side, where airflow separation can influence the airflow well beyond one wavelength (see again Fig. 8c).

Below the crest of the steep middle wave, we observe regions of intense turbulent stress (Panel e). Just past the bulge, a small region of intense negative turbulent stress is visible, which decays rapidly with depth. Intense positive turbulent shear stress is found along and below the upwind face of the crest, and up to the end of the bulge.

We note that the intense vorticity and turbulence observed under the steep wave's crest confirm that this wave is microscale breaking. As mentioned above, this was also suggested by the appearance of parasitic capillaries an instant later.

The derived surface viscous stress (Fig. 9f) is consistent with the air-side observations, being high below the crests and low below the troughs. The peak is particularly visible below the toe, likely because of the high shear region present here. The viscous stress notably drops below zero downwind of the bulge, an indicator that airflow separation is likely taking place over this microscale breaking wave.

4 Conclusions

A new laser imaging system was developed for the study of wind-wave interactions, combining a large, 51-cm-wide 2D PIV field of view with LIF water surface elevation measurements. The system provides high-resolution velocity maps above and below the water surface, with a resolution of one velocity vector every $133 \mu\text{m}^2$ and at a rate of 11 fields per second.

The system was deployed within University of Hamburg's large wind-wave facility, at a fetch of 15.5 m, and tested for wind-generated waves with a reference wind speed of 4.5 m/s. In these conditions, we are able, for the first time, to capture 2D snapshots of airflow dynamics above, and water dynamics below, a train of three to four wind waves at a time.

We are able to examine the details of the flow above and below microscale breaking waves, and their associated parasitic capillary waves, as well as flow features produced by interactions between several waves of a same wave group. The observed dominant waves, as they travel through the group, generally become steep enough to microscale break, produce capillaries past their crests and cause airflow separation events. This is accompanied by enhanced turbulence both under the wave crest and within the air-side sheltered region. High vorticity layers detach from the surface on the

air side, and intense vorticity is observed below the microscale breaking wave crests. Finally, we are able to follow the evolution of individual waves and their surrounding flow. Importantly, this provides the first direct evidence of instances where airflow separation events and their associated increased airflow variability can extend well beyond the first wave downwind, therefore strongly affecting the wind stress on the surface, over a distance of several wavelengths. These novel high-resolution, wide-field-of-view measurements offer the potential to examine a number of important questions, e.g., on the development of microscale breaking waves and associated capillaries within wave groups, and the along-group modulations of air and water turbulent processes, under various wind and wave conditions.

Acknowledgements This research was supported by the project "Biogeochemical processes and Air-sea exchange in the Sea-Surface microlayer (BASS)," which was funded by the German Research Foundation (DFG) under Grant No 451574234. We thank Daniel Blandfort for his help with the segmentation algorithm used to automatically detect the water surface.

Author contributions C.T., M.P.B., and M.G. developed the experiment. C.T. and J.M.M. conducted the experiments. C.T. performed the data analysis. C.T. and M.P.B. directed and composed the manuscript. All authors reviewed the manuscript.

Funding Open Access funding enabled and organized by Projekt DEAL.

Data availability Data sets generated during the current study are available from the corresponding author on reasonable request.

Declarations

Conflict of interest The authors declare no conflict of interest.

Open Access This article is licensed under a Creative Commons Attribution 4.0 International License, which permits use, sharing, adaptation, distribution and reproduction in any medium or format, as long as you give appropriate credit to the original author(s) and the source, provide a link to the Creative Commons licence, and indicate if changes were made. The images or other third party material in this article are included in the article's Creative Commons licence, unless indicated otherwise in a credit line to the material. If material is not included in the article's Creative Commons licence and your intended use is not permitted by statutory regulation or exceeds the permitted use, you will need to obtain permission directly from the copyright holder. To view a copy of this licence, visit <http://creativecommons.org/licenses/by/4.0/>.

References

- Banner ML, Melville WK (1976) On the separation of air flow over water waves. *J Fluid Mech* 77:825–842
- Banner ML, Peirson WL (1998) Tangential stress beneath wind-driven air-water interfaces. *J Fluid Mech* 364:115–145
- Banner ML, Phillips O (1974) On the incipient breaking of small scale waves. *J Fluid Mech* 65(04):647–656
- Belcher SE, Hunt JCR (1998) Turbulent flow over hills and waves. *Annu Rev Fluid Mech* 30:507–538

- Buckley MP, Horstmann J, Savelyev I, Carpenter JR (2025) Direct observations of airflow separation over ocean surface waves. *Nat Commun* 16:5526. <https://doi.org/10.1038/s41467-025-61133-1>
- Buckley MP, Veron F (2016) Structure of the airflow above surface waves. *J Phys Oceanogr* 46(5):1377–1397
- Buckley MP, Veron F (2017) Airflow measurements at a wavy air-water interface using PIV and LIF. *Exp Fluids* 58(11):161
- Buckley MP, Veron F (2019) The turbulent airflow over wind generated surface waves. *Eur J Mech* 58(11):161
- Buckley M, Veron F, Yousefi K (2020) Surface viscous stress over wind-driven waves with intermittent airflow separation. *J Fluid Mech* 905:31
- Buckley MP (2015) Structure of the airflow above surface waves. Phd dissertation, University of Delaware
- Cheung TK, Street RL (1988) The turbulent layer in the water at an air water interface. *J Fluid Mech* 194:133–151
- Deike L, Popinet S, Melville WK (2015) Capillary effects on wave breaking. *J Fluid Mech* 769:541–569
- Ebuchi N, Kawamura H, Toba Y (1987) Fine structure of laboratory wind-wave surfaces studied using an optical method. *Bound-Layer Meteorol* 39(1–2):133–151
- Gade M, Alpers W, Ermakov SA, Hühnerfuss H, Lange PA (1998) Wind-wave tank measurements of bound and freely propagating short gravity-capillary waves. *J Geophys Res Oceans* 103(C10):21697–21709
- Gent P, Taylor P (1976) A numerical model of the air flow above water waves. *J Fluid Mech* 77(1):105–128
- Jeffreys H (1925) On the formation of water waves by wind. *Proc R Soc* 107(742):189–206. <https://doi.org/10.1098/rspa.1925.0015>
- Jessup AT, Zappa CJ, Loewen MR, Hesany V (1997) Infrared remote sensing of breaking waves. *Nature* 385:52–55
- Kirillov A, Mintun E, Ravi N, Mao H, Rolland C, Gustafson L, Xiao T, Whitehead S, Berg AC, Lo W-Y (2023) Segment anything. In: Proceedings of the IEEE/CVF international conference on computer vision, pp 4015–4026
- Kundu PK, Cohen IM (2004) Fluid Mech, 3rd edn. Academic Press, Amsterdam
- Lobemeier P (1981) A wire probe for measuring high frequency sea waves. *J Phys E: Sci Instrum* 14(12):1407
- Longuet-Higgins MS (1963) The generation of capillary waves by steep gravity waves. *J Fluid Mech* 16(01):138–159
- Longuet-Higgins MS (1963) The effect of non-linearity on statistical distributions in the theory of sea waves. *J Fluid Mech* 17(3):459–480. <https://doi.org/10.1017/S0022112063001452>
- Longuet-Higgins MS (1992) Capillary rollers and bores. *J Fluid Mech* 240:659–679
- Melville WK (1983) Wave modulation and breakdown. *J Fluid Mech* 128:489–506
- Melville WK, Fedorov AV (2015) The equilibrium dynamics and statistics of gravity-capillary waves. *J Fluid Mech* 767:449–466
- Pearson WL (1997) Measurement of surface velocities and shears at a wavy air-water interface using particle image velocimetry. *Exp Fluids* 23:427–437
- Reul N, Branger H, Giovanangeli J-P (1999) Air flow separation over unsteady breaking waves. *Phys Fluids* 11:1959–1961
- Reul N, Branger H, Giovanangeli J-P (2008) Air flow structure over short-gravity breaking water waves. *Bound-Layer Meteorol* 126:477–505
- Reul N (1998) Etude expérimentale de la structure de l'écoulement d'air au-dessus de vagues courtes déferlantes. Phd dissertation, Univ. de la Mediterranee, Marseille
- Siddiqui MHK, Loewen MR (2007) Characteristics of the wind drift layer and microscale breaking waves. *J Fluid Mech* 573:417–456. <https://doi.org/10.1017/S0022112006003892>
- Siddiqui K, Loewen M (2010) Phase-averaged flow properties beneath microscale breaking waves. *Bound-Layer Meteorol* 134:499–523. <https://doi.org/10.1007/s10546-009-9447-6>
- Siddiqui MHK, Loewen MR, Asher WE, Jessup AT (2004) Coherent structures beneath wind waves and their influence on air-water gas transfer. *J. Geophys Res-Oceans* 109:03024
- Siddiqui MHK, Loewen MR, Richardson C, Asher WE, Jessup AT (2001) Simultaneous particle image velocimetry and infrared imagery of microscale breaking waves. *Phys Fluids* 10(1063/1):1375144
- Sullivan PP, McWilliams JC (2010) Dynamics of winds and currents coupled to surface waves. *Annu Rev Fluid Mech* 42:19–42
- Sullivan PP, McWilliams JC, Moeng C (2000) Simulation of turbulent flow over idealized water waves. *J Fluid Mech* 404:47–85. <https://doi.org/10.1017/S0022112099006965>
- Tenhaus J, Buckley MP, Matt S, Savelyev IB (2024) Viscous and turbulent stress measurements above and below laboratory wind waves. *Exp Fluids* 65(12):174
- Thomas M, Misra S, Kambhamettu C, Kirby JT (2005) A robust motion estimation algorithm for PIV. *Meas Sci Technol* 16(3):865–877. <https://doi.org/10.1088/0957-0233/16/3/031>
- Veron F, Saxena G, Misra SK (2007) Measurements of the viscous tangential stress in the airflow above wind waves. *Geophys Res Lett* 34:L19603. <https://doi.org/10.1029/2007GL031242>
- Wunsch C, Ferrari R (2004) Vertical mixing, energy, and the general circulation of the oceans. *Annu Rev Fluid Mech* 36:281–314
- Xu C, Perlin M (2023) Parasitic waves and micro-breaking on highly nonlinear gravity-capillary waves in a convergent channel. *J Fluid Mech* 962:46
- Zeiler A, Faltermeier R, Keck IR, Tomé AM, Puntonet CG, Lang EW (2010) Empirical mode decomposition—an introduction. In: The 2010 international joint conference on neural networks (IJCNN). IEEE, pp 1–8

Publisher's Note Springer Nature remains neutral with regard to jurisdictional claims in published maps and institutional affiliations.